Proceedings of the Canadian Society for Mechanical Engineering International Congress
Computational Fluid Dynamics Canada International Congress
CSME - CFD-SC2025
May 25-28, 2025, Montréal, QC, Canada

Noise prediction of a Controlled Diffusion airfoil at high angle-of-attack

Andrea Arroyo Ramo[1,2], Clara G. Morency[1], Stéphane Moreau[1], Michaël Bauerheim[2], Richard D. Sandberg[3]

[1]Faculté de Génie, Université de Sherbrooke Sherbrooke, Canada
[2]Département Aérodynamique, Énergetique et Propulsion, ISAE-Supaero, Toulouse, France
[3]Department of Mechanical Engineering, the University of Melbourne, Melbourne, Australia

***Abstract*—**Direct Numerical Simulations (DNS) of the compressible flow over a Controlled Diffusion (CD) airfoil are conducted at a high geometrical angle-of-attack of 15°. To obtain far field noise predictions, the compressible DNS results are coupled with the Ffowcs Williams & Hawkings acoustic analogy. The mean installation effects associated with open-jet anechoic wind tunnel conditions are included in the computations. A large flow separation with a large coherent structure shedding is observed in the front part of the airfoil, followed by a re-attachment at mid-chord, and a second flow detachment downstream. Similar to the work previously conducted on the 8° case, three noise sources have been found: the flow separation and reattachment; the interaction between the attached turbulent flow at the trailing edge; and a secondary instability in the near wake. Yet, the first noise source is predominant at a high angle-of-attack of 15°
.

***Keywords-component*—CFD, DNS, Aeroacoustics, Airfoil noise**

I. Introduction

Noise is a general concern in most industrial applications. In particular, it is a major annoyance in turbomachinery appliances such as engine cooling fans, wind turbines or high-speed turbo engines. Among all noise sources in a rotating machine, blade, or airfoil, self-noise is an important contributor to the total noise emitted, since it corresponds to the minimum achievable noise level. In fact, this broadband noise source can become dominant when other interaction sources are absent. It is typically caused by the interaction between turbulent eddies in the turbulent boundary layer and in the wake, and the airfoil itself. Yet, under off-design conditions, which is the focus of the present study, the broadband noise can be generated not only by the interaction of the turbulent flow field with the airfoil, but also by the large turbulent coherent structures shed at high angle-of-attack.

EUR-TSAE,NSERC

Numerical predictions of airfoil self-noise have recently been reviewed in [1]. From all the methods presented, the hybrid approach based on the acoustic formulation of Ffowcs Williams & Hawkings [2] is used to study airfoil self-noise in the present work. The latter follows trends from the last decade, in which high-fidelity compressible simulations (Large Eddy Simulations –LES– [3], [4], and Direct Numerical Simulations –DNS– [5]–[8]) have been used to perform predictions of trailing-edge noise. The high-fidelity simulations are coupled with an acoustic solver to propagate the acoustics resolved in the near-field towards the far-field. However, except for [9], every simulation mentioned has focused on attached flow conditions at low to moderate angle-of-attack.

The objective of the present work is to investigate the turbulent flow field and the contribution of different noise sources to the airfoil noise at high angle-of-attack. It has already been observed under design conditions that not only the trailing edge, but also the laminar-turbulent transition region, are efficient noise sources [10], [11]. Indeed, the trailing-edge noise was found to contribute at all frequencies, whereas transition/reattachment region at the leading edge had an effect on the high frequencies. The present study aims at extending this survey to off-design conditions.

The present DNS is carried out on a Controlled Diffusion (CD) airfoil, a cambered airfoil used in industrial applications such as turbo-engine compressor and fan blades, as well as automotive engine cooling fans. The numerical results are validated with experimental data in open-jet anechoic wind tunnels [12]. To do so, the simulation must include the flow conditions found in such test facilities [13]. Thus, the airfoil must be immersed in the potential core of the jet. Because of these installation effects, the flow around the airfoil becomes non-uniform; the airfoil loading, boundary layer development, and flow separation are altered, which leads to a modification of the sound field [14]. The present study focuses on a high

geometric angle-of-attack of 15°, at a Reynolds number of 1.5×10^5 and a Mach number of 0.25.

II. Numerical modeling

A 3D DNS of the flow over the CD airfoil with a chord $c = 0.1356$ m, embedded in the jet potential core of a free-jet wind tunnel, is conducted at a chord-based Reynolds number of $Re_c = 1.5 \times 10^5$; a free-stream Mach number of $M = 0.25$; a geometric angle-of-attack of 15°; and reference velocity of $U_\infty = 16$.

A. Flow field model

The dynamics of the flow are described by the non-dimensionalized fully compressible Navier-Stokes equations, which include the conservation of mass, momentum, and energy. The reference quantities used for normalization are the chord length of the airfoil, the free-stream velocity, density, and temperature. To close the system of equations, the non-dimensional form of the state equation with a ratio of specific heats $\gamma = 1.4$ is applied. The set of equations is found in [15].

The numerical code employed to carry out the simulation is *HiPSTAR* [14]. Further details of the solver are found in [15]. The CD airfoil computations have been carried out on a reduced rectangular domain, as seen in Fig. 1. It allows the airfoil to be embedded in the core of the jet (see Fig. 2). The structured mesh is composed of three overlapping blocks: a background mesh (Block 1); a superimposed O-grid around the airfoil (Block 2); and a refinement region in the near wake or "fishtail" (Block 3). The O-grid and near wake blocks allow for high-quality refinement around the airfoil, thus properly resolving the laminar and turbulent boundary layers.

After a refinement around the airfoil surface of the mesh used in previous studies at low incidence angle [16], the composition of the O-grid and near wake meshes consists of 2958×336 grid points in the tangential and normal directions from the airfoil surface, respectively. The near wake is then further extended 645 points downstream. A total of 192 spanwise spectral modes cover the spanwise length of $0.2c$. This spanwise extent was proven to be sufficiently large [17].

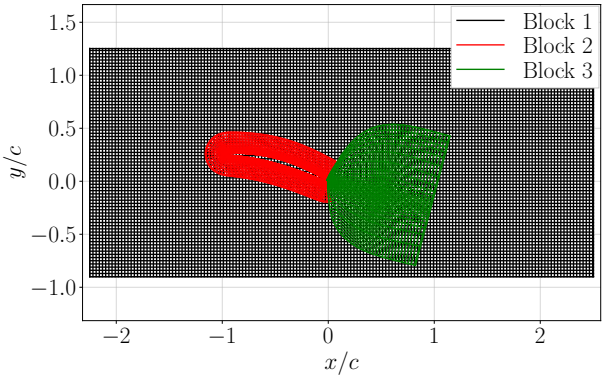

Figure. 1: Slice of complete domain meshing. Two-block structured mesh fitting the core of the jet. Every 15 gridlines of mesh shown.

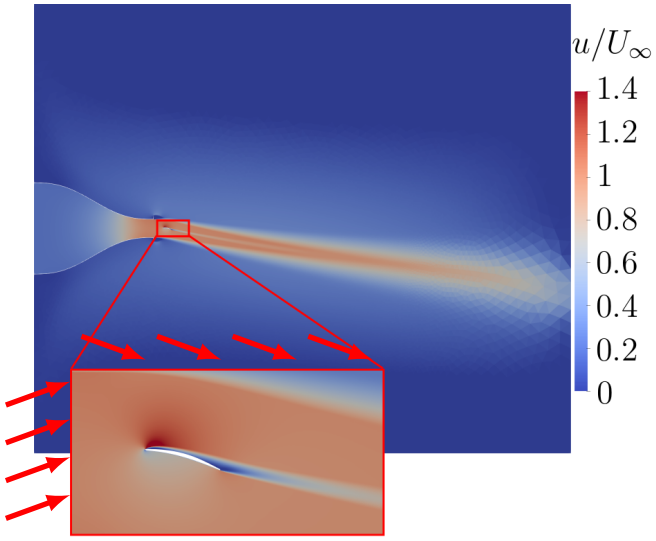

Figure. 2: Velocity contours of the full wind tunnel 2D RANS calculation employed as initialization and boundary values in the DNS. Reduced DNS domain in red rectangle. Boundary inflow velocity profiles depicted by red arrows.

The computational stability is ensured by setting a dimensionless time step of 4.25×10^{-6}, which corresponds to a physical time step of 3.6×10^{-8} s. This time step provides a CFL < 1 in the domain. Finally, in the wall-normal direction, $y^+ < 1$ over most of the airfoil surface, with its maximum value $y^+_{\max} \approx 1.7$ at the leading edge. In addition, the normalized crosswise and spanwise wall distances are $x^+ \approx z^+ < 8$ on the surface, except for the leading edge, where the values spike up to 40 units.

The boundary conditions used in the DNS reproduce the mean experimental conditions observed in open-jet facilities with a jet width of 50 cm, at École Centrale de Lyon (ECL) and at Université de Sherbrooke (UdeS). Compared to the free-field conditions, the installation effects produce a modification in the airfoil loading [12]. To include such effects, a 2D Reynolds-Averaged Navier-Stokes (RANS) simulation of the flow around the CD airfoil is first computed (see Fig. 2), and used in the DNS to introduce both the initial and boundary conditions. At each instant, the mean velocity profiles are imposed in the corresponding simulation boundaries, as depicted in Fig. 2.

B. Acoustic field model

The DNS solves both aerodynamics and acoustics close to the airfoil. Therefore, to compute the acoustic radiation produced by the CD airfoil, an acoustic propagator is required. Thus, the DNS results are coupled with the in-house Ffowcs-Williams & Hawkings (FWH) solver, *SherFWH*. The far-field acoustic pressure consists of two principal components: monopolar (related to thickness noise) and dipolar (related to loading noise), which correspond to the first and second terms in Eq. (1), respectively.

Both porous and solid formulations are used to compute the far-field noise. The airfoil surface is required for the solid

formulation, and an additional open surface surrounding the airfoil is used in the porous formulation. These control surfaces are used to enclose the considered noise sources. Finally, the wall-pressure fluctuations are sampled at a frequency of approximately 111 kHz.

$$p'(\mathbf{x},t) = \frac{\partial}{\partial t}\int_{f=0}\left[\frac{Q_i n_i}{4\pi|\mathbf{x}-\mathbf{y}|}\right]_{\tau_e} \mathrm{d}S - \frac{\partial}{\partial x_i}\int_{f=0}\left[\frac{L_{ij} n_j}{4\pi|\mathbf{x}-\mathbf{y}|}\right]_{\tau_e} \mathrm{d}S \tag{1}$$

III. Results

In this section, the results for the high angle-of-attack CD airfoil under specified conditions are presented. First, the aerodynamic field is measured to show the fidelity level of the simulation with respect to the experiments. After, the aeroacoustic field is evaluated. Several complex physical phenomena occur in the flow passing over the suction side of a CD airfoil, as seen in Fig. 3: leading-edge laminar separation; laminar-turbulent transition leading to flow reattachment; and finally, the flow leaving the airfoil at the trailing edge producing a small trailing-edge vortex shedding. Details on the laminar separation bubble (LSB) are also found in Fig. 3. The laminar region on the suction side is shorter compared to the low incidence case [15], triggering an earlier turbulent transition and a thicker and longer LSB. In addition, the pressure side remains fully laminar up to the position where the vortex shedding occurs at the trailing edge.

The time and spanwise averaged wall-pressure and wall-friction coefficients are defined in Eq. (2). The reference free-stream density ρ_∞, velocity U_∞, and pressure p_∞ are used to normalize the time- and spanwise-averaged wall-pressure and friction distributions $\langle p\rangle$ and $\langle \tau_w\rangle$, respectively.

$$C_p = \frac{\langle p\rangle - p_\infty}{1/2\rho_\infty U_\infty^2} \quad , \quad C_f = \frac{\langle \tau_w\rangle}{1/2\rho_\infty U_\infty^2} \tag{2}$$

The wall-pressure coefficient is shown in Fig. 4, where it is compared to experimental data at various positions along the chord using Remote Microphone Probes (RMP). Also presented is an additional DNS carried out by Zhou *et al.* [18] using the Lattice Boltzmann Method (LBM) and an earlier incompressible Large Eddy Simulation (LES) achieved by Christophe *et al.* [19]. Both additional simulations also include the installation effects. In particular, the LBM includes the complete geometry found in the wind tunnel experiments. The

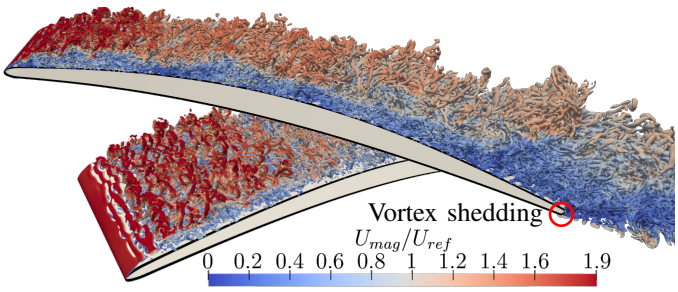

Figure. 3: Instantaneous field of λ_{ci}-criterion, velocity magnitude. Leading-edge detail, DNS results. Red circle defining the trailing-edge vortex shedding position.

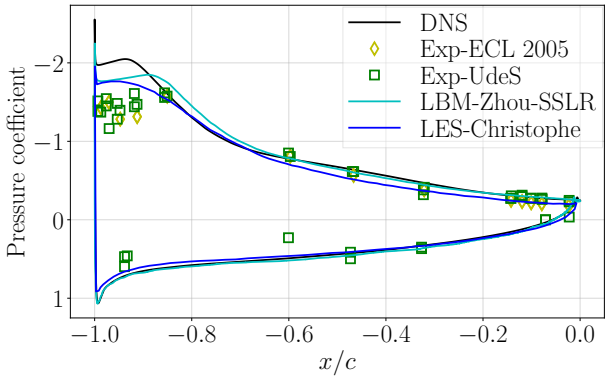

Figure. 4: Temporal and spanwise mean value of the wall-pressure coefficient C_p

suction side is characterized by two distinguished regions: the LSB, followed by the adverse pressure gradient. An overall agreement is found in the size of the LSB numerically as well as in the experiments. The wall-friction coefficient found in Fig. 5 provides the size of the LSB: it covers around 30% of the airfoil. In addition, the positive value of C_f indicates that the flow remains attached almost up to the trailing edge, where C_f becomes negative, indicative of the turbulent flow detachment.

The mean tangential velocity profiles on multiple locations on the suction side are represented in Fig. 6). The tangential velocity U_t is normalized by the maximum tangential velocity found in the mean velocity profile $U_{t,max}$, whereas the normal distance to the wall h is normalized by the airfoil chord c. The selected positions are found within the LSB; at the midchord; and two positions at the trailing edge (RMP 26 is found at the last 2% of the chord). The data is compared to the LBM simulation of Zhou *et al.* [18]. RMP 3 is completely immersed inside the LSB, as evidenced by the negative value of the tangential velocity. Moving slightly downstream, at RMP 5 (not represented here), the LSB is thicker in the LBM simulation. As the adverse pressure gradient effects become progressively more important, the thickness of the boundary layer increases, as seen progressively at RMPs 9, 21, and 26.

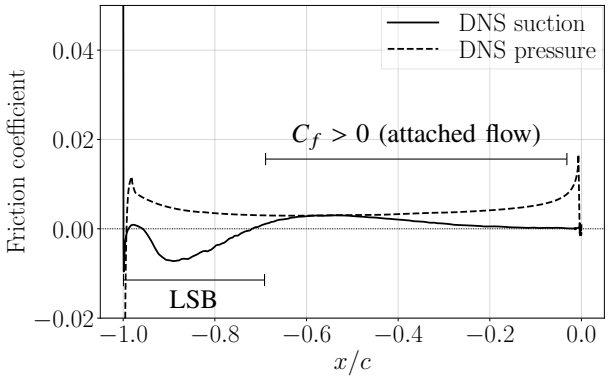

Figure. 5: Temporal and spanwise mean value of the wall-friction coefficient C_f

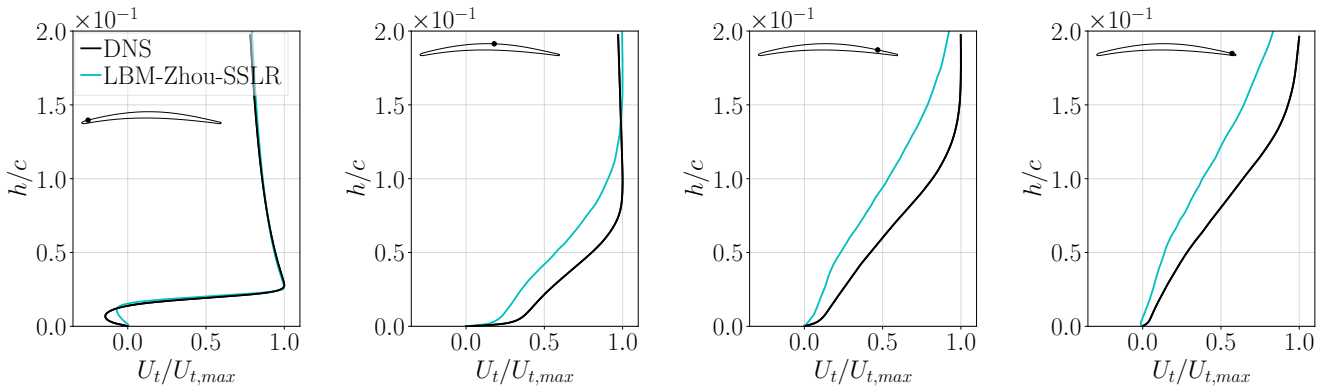

(a) RMP 3. (b) RMP 9. (c) RMP 21. (d) RMP 26.

Figure. 6: Suction side mean tangential velocity profiles above RMPs along the airfoil suction side. DNS compared to LBM data extracted from Zhou *et al.* [18].

Note that the overall thickness of the boundary layer is larger in the LBM case. In LBM case, since the complete geometry found in experiments is simulated, there is no restriction on the core of the jet evolution in the simulation, whereas in the current DNS, the boundary conditions are stationary. It produces a confinement effect in the simulation, restricting possible flapping of the jet shear layers as found in [20].

The spanwise-average power spectral density (PSD) $\phi_{pp}(\omega)$ of the wall-pressure fluctuations p' at a given frequency ω are obtained by using Eq. (4):

$$R_{pp}(\xi_x, \xi_z, \tau) = \lim_{T\to\infty} \frac{1}{T} \int_0^T p'(x, z, t) p'(x + \xi_x, z + \xi_z, t + \tau) \mathrm{d}t \tag{3}$$

$$\phi_{pp}(\omega) = \frac{1}{2\pi} \int_{-\infty}^{\infty} R_{pp}(0, 0, \tau) \mathrm{e}^{-\mathrm{i}\omega\tau} \mathrm{d}t \tag{4}$$

The results for the wall-pressure spectra, at the same locations as in the previous boundary layer velocity profiles are presented in Fig. 7. The results are represented in decibels,

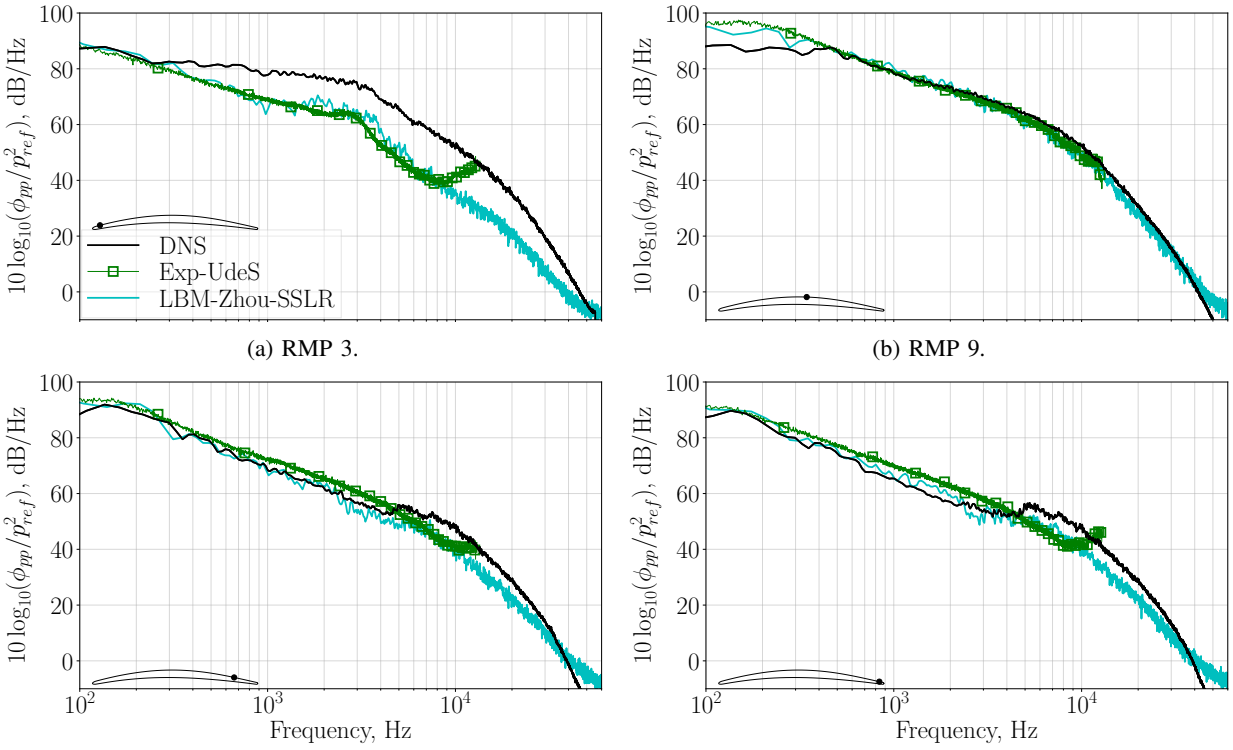

(a) RMP 3. (b) RMP 9.

(c) RMP 21. (d) RMP 26.

Figure. 7: Suction side spanwise-averaged PSD of wall-pressure fluctuations at different RMP locations. $p_{ref} = 2 \times 10^{-5}$ Pa. DNS compared to experimental and LBM data extracted from Zhou *et al.* [18].

using as reference pressure p_{ref} the human hearing threshold for their normalization. The data is compared with the aforementioned LBM, as well as with UdeS experiments. The major discrepancies occur in the LSB region (RMP 3, Fig. 7a), where the associated spectrum levels from the current DNS are larger than the ones found in the experiments or in the LBM simulation. This overprediction of the levels is not surprising since the wall-pressure coefficient in the LSB region (Fig. 4) is larger in the present computation than in other numerical and experimental data, further stressing leading-edge flow acceleration and increasing the LSB intensity. Nevertheless, the hump associated with the LSB is found around 2-4 kHz for all the cases. At mid-chord (RMP 9, Fig. 7b), similar results are found in both simulations and experiments. Close to the trailing edge, all the results provide a general good agreement. Moving closer to the trailing edge (RMP 26, Fig. 7d), a high-frequency hump appears around 5-10 kHz. In the experiments, there is a hint of such a hump at frequencies above 10 kHz, whereas in the LBM, it is almost unnoticeable, with only a slight slope reduction around 3-8 kHz. This hump was also observed in the 8° CD airfoil simulation and is attributed to the acoustic imprint on the wall of a noise source found downstream of the trailing edge [16].

The instantaneous dilatation field $-\partial\rho/\partial t$ shown in Fig. 8 provides noise sources close to the airfoil. The instantaneous contours of the λ_{ci}-criterion are colored by the velocity magnitude and are superimposed on the dilatation field. The dilatation field is evaluated at multiple frequency ranges to evaluate which sources are found for each frequency range. To do so, the time derivative of the density field is first Fourier transformed to obtain its evolution in the frequency domain. A band pass filter is applied after only evaluating the desired range of frequencies. Then, the inverse Fourier transform is applied to the data to retrieve the temporal evolution. The low-frequency regime (Fig. 8a) presents the main noise source at the trailing edge, and a secondary contribution at the leading edge (LSB). In the mid-high-frequency regime (Fig. 8b) two sources appear: the LSB and the trailing edge source. In the high-frequency regime (Fig. 8c), three main noise sources are found: the LSB at the leading edge; the near wake source (the noise source downstream the trailing edge) ;and finally, the noise associated with the jet shear layer. In the unfiltered field (Fig. 8d), the addition of all noise sources is found, including the merge of the trailing edge and near wake sources to create an elliptical noise source downstream the trailing edge.

Finally, the noise spectrum at 90° and at a distance of 2 m from the trailing edge is shown in Fig. 9. The far field prediction has been carried out with the FWH propagator using both the airfoil wall (solid black) and the porous control surface (solid blue). They are compared to the experiments of UdeS and ECL, as well as to the FWH solid formulation on the LBM [18]. The results from the incompressible LES [19] were obtained with Amiet's extended model valid for an airfoil assimilated to a finite-chord flat plate with no thickness [21]. The results of the current simulation, as well as that of the LBM, significantly improve the previous LES results, but produce an overprediction of the sound pressure levels, i.e. frequencies are above 2 kHz compared to the experiments. This is most likely related to the Mach number sensitivity on the sound pressure level, since an additional LBM at Mach

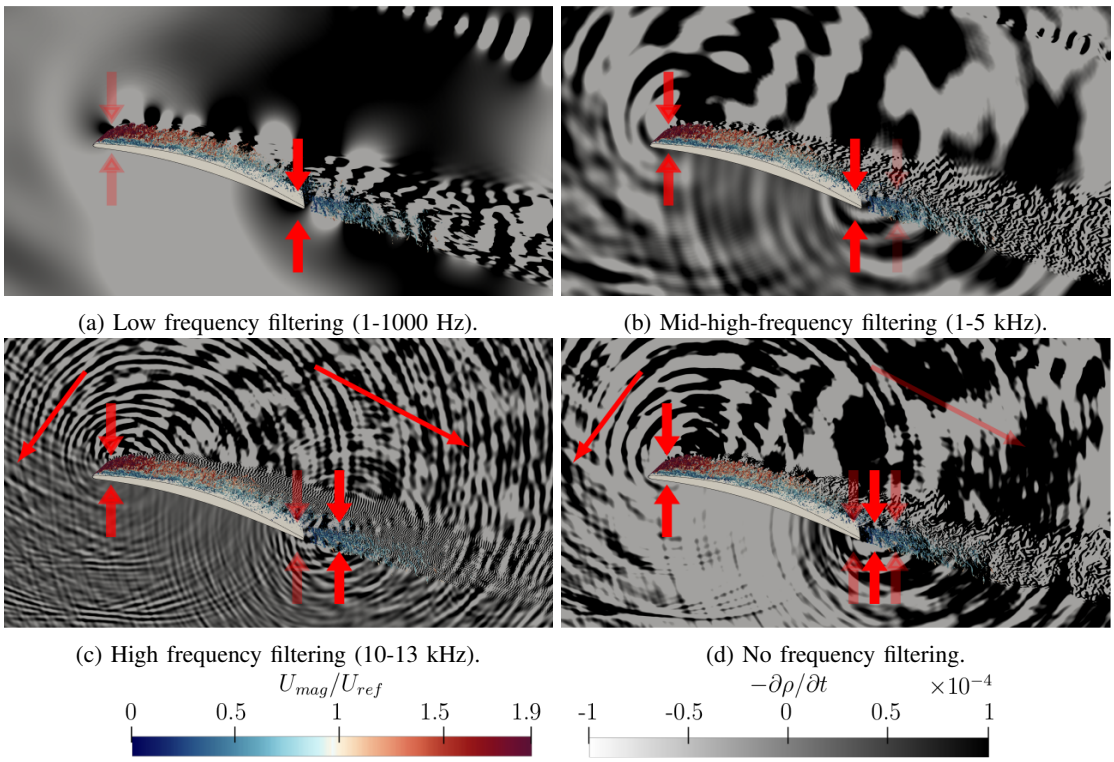

(a) Low frequency filtering (1-1000 Hz).

(b) Mid-high-frequency filtering (1-5 kHz).

(c) High frequency filtering (10-13 kHz).

(d) No frequency filtering.

Figure. 8: Instantaneous field of λ_{ci}-criterion velocity magnitude superimposed on the dilatation field contours $-\partial\rho/\partial t$. Filtering at various frequency ranges. Red arrows pointing at the sound source positions.

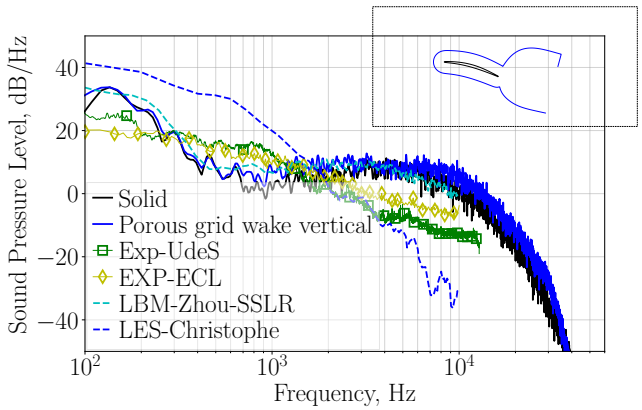

Figure. 9: Sound Pressure Levels at 2 m from the trailing edge, at 90° on the suction side. Surfaces used in the FWH propagation represented inside the DNS domain on the top-right.

0.1 carried out by Zhou *et al.* [18] shows a better agreement with experiments achieved at $M = 0.06$.

IV. Conclusion

A compressible DNS of the flow over a Controlled Diffusion airfoil at a geometric angle-of-attack of 15°, a chord-based Reynolds number $Re_c = 1.5 \times 10^5$ and a free-stream Mach number $M = 0.25$ has been carried out to study the relationship between the near-field and far-field pressure and how it relates to noise generation mechanisms. In order to properly validate the numerical results with experimental data, the installation effects are included in the simulations.

The aerodynamic results show compliance with the experiments at ECL and UdeS. The computed wall-pressure and friction coefficients confirm the presence of a laminar separation bubble covering about 30% of the suction side. The mean boundary layer velocity profile compared with the LBM including the actual experimental set-up stresses the importance of including the jet effect in the simulation, as it modifies the boundary layer extension.

The far-field noise is predicted using the FWH acoustic analogy. The results are similar to that of the LBM simulation including the full experimental set-up. The filtered dilatation field shows three main noise sources for the CD airfoil at high angle-of-attack:

1) the laminar separation bubble on the suction side produced by the flow separation and reattachment at the leading edge (dominant noise source in the far-field acoustic spectra, present at all frequencies);
2) the interaction between the suction-side turbulent eddies convected downstream and the airfoil trailing edge; and
3) the interaction of turbulent eddies in the near wake downstream of the trailing edge.

These noise sources are similar to those reported at 8° angle-of-attack, but with a dominant leading-edge noise radiation.

Acknowledgment

This work was partly supported by the French "Programme d'Investissements d'avenir" EUR-TSAE. We also acknowledge the support of the Natural Sciences and Engineering Research Council of Canada (NSERC). This work was performed using HPC resources from GENCI–IDRIS (Grant 2024-103368).

References

[1] S. Lee, L. Ayton, F. Bertagnolio, S. Moreau, T. P. Chong, and P. Joseph, "Turbulent boundary layer trailing-edge noise: Theory, computation, experiment, and application," *Prog. Aerosp. Sci*, vol. 126, no. June, p. 100737, 2021.

[2] J. E. Ffowcs-Williams and L. H. Hall, "Aerodynamic sound generation by turbulent flow in the vicinity of a scattering half plane," *J. Fluid Mech*, vol. 40, no. 4, pp. 657–670, 1970.

[3] R. Boukharfane, M. Parsani, and J. Bodart, "Characterization of pressure fluctuations within a controlled-diffusion blade boundary layer using the equilibrium wall-modelled LES," *Scientific Reports*, vol. 10, pp. 1–19, March 2020.

[4] M. Deuse and R. D. Sandberg, "Different noise generation mechanisms of a controlled diffusion aerofoil and their dependence on Mach number," *J. Sound Vib*, vol. 476, p. 115317, March 2020.

[5] R. D. Sandberg, N. D. Sandham, and P. F. Joseph, "Direct numerical simulations of trailing-edge noise generated by boundary-layer instabilities," *J. Sound Vib*, vol. 304, pp. 677–690, March 2007.

[6] M. Sanjosé, S. Moreau, M. S. Kim, and F. Pérot, "Direct self-noise simulation of the installed Controlled Diffusion airfoil," in *Proceedings of the 17th AIAA/CEAS Aeroacoustics Conference*, 2011-2716, (25-29 June, Portland, Oregon (USA)), June 2011.

[7] J. Winkler., H. Wu, S. Moreau, T. Carolus, and R. Sandberg, "Trailing-edge broadband noise prediction of an airfoil with boundary-layer tripping," *J. Sound Vib*, vol. 482, pp. 115450:1–25, 2020.

[8] H. Wu, S. Moreau, and R. Sandberg, "On the noise generated by a controlled-diffusion aerofoil at $Re_c = 1.5 \times 10^5$," *J. Sound Vib*, vol. 506, pp. 116152: 1–20, 2020.

[9] J. M. Turner and J. W. Kim, "Quadrupole noise generated from a low-speed aerofoil in near-and full-stall conditions," *J. Fluid Mech*, vol. 936, p. A34, 2022.

[10] R. D. Sandberg and N. D. Sandham, "Direct numerical simulation of turbulent flow past a trailing edge and the associated noise generation," *J. Fluid Mech*, vol. 596, p. 353–385, 2008.

[11] L. E. Jones, N. D. Sandham, and R. D. Sandberg, "Acoustic source identification for transitional airfoil flows using cross correlations," *AIAA J*, vol. 48, pp. 2299–2312, 2010.

[12] S. Moreau and M. Roger, "Effect of Airfoil Aerodynamic Loading on Trailing-Edge Noise Sources," *AIAA J*, vol. 43, pp. 41–52, January 2005.

[13] S. Moreau, M. Henner, G. Iaccarino, M. Wang, and M. Roger, "Analysis of Flow Conditions in Freejet Experiments for Studying Airfoil Self-Noise," *AIAA J*, vol. 41, pp. 1895–1905, October 2003.

[14] R. D. Sandberg, "Compressible-flow DNS with application to airfoil noise," *Flow Turbulence Combust*, vol. 95, pp. 211–229, May 2015.

[15] A. Arroyo Ramo, S. Moreau, R. D. Sandberg, and M. Bauerheim, "Acoustic far-field prediction of a Controlled Diffusion airfoil self-noise," in *Proceedings of the CSME-CFDSC International Congress*, (28-31 May, Sherbrooke, QC (Canada)), May 2023.

[16] A. Arroyo Ramo, S. Moreau, R. D. Sandberg, M. Bauerheim, and M. C. Jacob, "Controlled Diffusion airfoil self-noise, an acoustic far-field prediction," in *Proceedings of the AIAA Aviation 2023 Forum*, 2023-3505, (12-16 June, San Diego, CA (USA)), June 2023.

[17] M. Wang and P. Moin, "Computation of trailing-edge flow and noise using large-eddy simulation," *AIAA J*, vol. 38, pp. 2201–2209, January 2000.

[18] Z. Zhou, S. Moreau, and M. Sanjosé, "On the Noise Mechanisms of a Controlled Diffusion Airfoil at Pre-Stall," in *Proceedings of the 30th AIAA/CEAS Aeroacoustics Conference*, 2024-3067, (4-7 June, Rome (Italy)), June 2024.

[19] J. Christophe, J. Anthoine, and S. Moreau, "Trailing Edge Noise of a Controlled-Diffusion Airfoil ar Moderate and High Angle of Attack," in *Proceedings of the 15th AIAA/CEAS Aeroacoustics Conference*, 2009-3196, (11-13 May, Miami, Florida (USA)), May 2009.

[20] Z. Zhou, S. Moreau, and M. Sanjosé, "Installation effects on airfoil self-noise estimated by direct numerical simulations," *J. Sound Vib*, vol. 604, p. 118978, 2025.

[21] M. Roger and S. Moreau, "Back-scattering correction and further extensions of Amiet's trailing-edge noise model. Part 1: theory," *J. Sound Vib*, vol. 286, pp. 477–506, February 2005.